A Nonsmoothing Approach to the Estimation of Vessel Contours in Angiograms

Mário A. T. Figueiredo, *Member, IEEE*, and José M. N. Leitão

Abstract— **Accurate and fully automatic assessment of vessel (stenoses) dimensions in angiographic images has been sought as a diagnostic tool, in particular for coronary heart disease. In this paper, we propose a new technique to estimate vessel borders in angiographic images, a necessary first step of any automatic analysis system. Unlike in previous approaches, the obtained edge estimates are not artificially smoothed; this is extremely important since quantitative analysis is the goal. Another important feature of the proposed technique is that no constant background is assumed, this making it well suited for nonsubtracted angiograms. The key aspect of our approach is that continuity/smoothness constraints are not used to modify the estimates directly derived from the image (which would introduce distortion) but rather to elect (without modifying) candidate estimates. Robustness against unknown background is provided by the use a morphological edge operator, instead of some linear operator (such as a matched filter) which has to assume known background and known vessel shape.**

I. Introduction

ACCURATE automatic analysis of vessel morphology in digital (or digitized) angiographic images is a valuable and clinically important diagnostic tool. Particularly for coronariography, objective, verifiable, and reproducible quantitative analysis has been the goal of much research effort [2]–[5]. Underlying this search is the need to accurately assess the severity of arterial stenoses associated with coronary heart disease. It is clear that border location is a necessary and important first step of any automatic *quantitative coronary analysis* (QCA) system. This fact is independent from the technique adopted (densitometric or purely geometric [4]) to measure stenoses severity.

Current QCA systems rely on manual or automatic vessel contour estimation. Accuracy and reproducibility strongly suggest the adoption of automatic edge detection for which several techniques have been proposed. Most of them impose smoothness on the extracted vessel borders as a way of achieving robustness against the inherent difficulties of the problem which include weak contrast and *a priori* unknown vessel shape and background structure. However, smoothness is an important source of measurement errors. In this paper, we introduce a technique to locate the contours of a vessel segment which does not impose smoothness constraints, thus producing undistorted, i.e., not artificially smoothed, estimates. Moreover, by using morphological operators rather than linear edge detectors, our scheme is adequate to nonsubtracted angiograms since it does without any background flatness assumption. The described algorithm is meant as the first stage of a QCA system under development; nevertheless, it can be adopted to other applications.

Manuscript received June 20, 1994; revised December 12, 1994. A short version of this work was presented at the 1993 *IEEE Nuclear Science Syposium and Medical Imaging Conference*. The Associate Editor responsible for coordinating the review of this paper and recommending its publication was N. Ayache.

The authors are with the Instituto de Telecomunicações, and Departamento de Engenharia Electrotécnica e de Computadores, Instituto Superior Técnico, Lisboa, Portugal.

IEEE Log Number 9408766.

II. Previous Work

Several techniques have been proposed to automatically identify vessel contours in coronary angiographic images. To cope with the difficulties inherent to the problem (unknown image background, faint contrast, unknown vessel shape), most approaches use prior knowledge/constraints about vessel continuity and smoothness. Some recent examples include dynamic programming type search, as in the works of Pope *et al.* [6], Eichel *et al.* [7], Reiber *et al.* [2], and Fleagle *et al.* [5], and extended Kalman filter type prediction-correction tracking, as proposed in the work of Sun [8]. By adopting smoothness constraints, these techniques achieve robustness at the cost of yielding artificially smoothed (distorted) vessel edges. This may be a serious problem if quantitative analysis is to be performed with the obtained vessel edges. Diameters in a typical coronariography can be of the order of a few pixels, with a one-pixel deviation then being a serious relative error. As an example, take the case of a very short but very pronounced narrowing (stenosis) which can be severely underestimated if any smoothness constraint is imposed on the edges fitted to it. This is in contrast with the ventricular boundary estimation problem in which the much larger dimensions involved give sense to simple smoothness constraints [9].

Other types of approaches, such as those of Bresler *et al.* [10], and Rossi *et al.* [11], are useless for coronary arteriograms because they assume constant (or known) background, and several projections, which are conditions seldom met in a realistic clinical setting.

An exception to the smoothness assumption trend is the work of Pappas and Lim [12], in which each vessel cross-section is analyzed separately. However, that work presents (from our point of view) some problems: the vessel and background models are simplistic and unrealistic, e.g., the background is modeled as a low-order polynomial; by performing section-by-section independent analysis, smoothness is avoided but the robustness that is typical of global approaches, i.e., in which all border points are jointly estimated, is thrown away.

Matched filter techniques, as used by Nichols *et al.* [13], Parker *et al.* [14], and Sun [8], and also first and/or second derivative (or gradient) based approaches used by most authors (such as [2], [5], [15]–[18], among others) can not be justified in the presence of arbitrary background and unknown vessel profile shape.

Recent work using a morphological approach to vessel extraction/enhancement in medical images (magnetic resonance angiography—MRA) is the one of Vandermeulen *et al.* [19], where 3-D visualization of MRA is improved by enhancing the contrast of blood vessels using (3-D) morphological filters specially matched to that end. Our work departs from [19] in that our goal is to precisely determine border locations on a vessel segment under study, rather than to enhance the entire vascular structure.

III. Rationale of the Proposed Method

The design goals herein adopted are: keep the robustness inherent to global approaches, i.e., do not treat each cross-section separately, taking advantage of contextual information provided by the surrounding estimates, while at the same time avoiding the distortion introduced by smoothness constraints; also, do not assume any background or vessel shape model.

The following observations and ideas underlie our method:

1) Even at low contrast vessel segments, e.g., stenotic areas and in the vicinity of (possibly stronger) image artifacts, e.g., ribs, other vessels, and catheters, any edge operator still presents a (possibly weak) local maximum at the correct border location.
2) This maximum can be correctly picked up if the surrounding contextual information is somehow adequately taken into account.
3) Continuity (or smoothness) constraints should not be used to modify the edge location estimates directly derived from the image.
4) The edge operator must not be supported on any background flatness and/or additive white noise assumptions; moreover, the exact intensity profile of the vessels cross-sections is unknown.

The strategy followed to achieve these goals is supported on two types of tools: morphological filters [20]–[23], and dynamic programming [24]. It can coarsely be described as follows:

1) We begin by considering observation 4). The constraint of unknown background and vessel model led to the adoption of a morphological gray scale edge operator [21]–[23]. The reasons for choosing a morphological (nonlinear) operator are: absence of flat background and white noise assumptions, and lack of knowledge about the exact vessel profile. These facts rule out any linear operator, such as matched filters or any derivative-based scheme. Morphological edge operators are sensitive to the variations associated with the vessel borders, over an arbitrary background, while exhibiting noise immunity [22], [23].
2) For each vessel cross-section, all local maxima of the morphological edge operator are taken as candidates to edge points; according to observation 1), the correct border points are contained in this set of candidates. Dynamic programming is then used to find a least cost path through the candidates, picking a pair from each cross-section. The adopted cost includes continuity/smoothness and morphological edge operator output intensity terms. In this way, the prior knowledge about the vessel continuity/smoothness is used to elect, among several candidates, the one that best fits into the global contour, without modifying the estimates provided by the edge operator, i.e., without introducing distortion.

In the above-mentioned references [5]–[7], dynamic programming is also used, although in a fundamentally different way: minimum cost paths are found not through sets of candidates, but through all the pixels in an edge strength image. Thus, the selected points may not coincide with maxima of the edge operator and are possibly biased estimates. In our algorithm, continuity is used only to select among several candidates without modifying them. Other related applications of dynamic programming in image processing can be found in [25]–[28].

IV. The Tools

A. Morphological Operators

1) Basic Operators: In this section, we describe the adopted morphological edge operator (1-D version) after briefly presenting the underlying basic morphological operators. Consider a real sequence $\mathbf{x} = \{x_i\}$, of infinite duration (for simplicity). The *gray scale dilation* [20], [21], of sequence $\mathbf{x}$ by the *structuring element* $\mathbf{b} = \{b_n, n = n_i, \cdots, n_f\}$, is the sequence denoted by $\mathbf{x} \oplus \mathbf{b}$ and defined as

$$\mathbf{x} \oplus \mathbf{b} = \{\max_{n=n_i, \cdots, n_f} (x_{i-n} + b_n)\}. \tag{1}$$

The *gray scale erosion* [20], [21], of sequence $\mathbf{x}$ by the structuring element $\mathbf{b} = \{b_n, n = n_i, \cdots, n_f\}$, denoted by $\mathbf{x} \ominus \mathbf{b}$, is the sequence defined as

$$\mathbf{x} \ominus \mathbf{b} = \{\min_{n=n_i, \cdots, n_f} (x_{i-n} - b_n)\}. \tag{2}$$

These morphological operators are termed *gray scale* to distinguish them from those which involve binary signals [20], [21]. Most gray scale morphological algorithms are built by combining the basic operators just mentioned: erosion and dilation.

Simpler versions of the *dilation* and *erosion* transformations arise when the structuring element is flat and centered around the zero index, $\mathbf{b} = \{0, n = -N, \cdots, N\}$. This particularization yields the following simpler gray scale morphological operations:

1) *flat dilation:*

$$\begin{aligned} \mathrm{FD}(\mathbf{x}, N) &= \mathbf{x} \oplus \{0, n = -N, \cdots, N\} \\ &= \{\max_{n=-N, \cdots, N} (x_{i-n})\}, \end{aligned}$$

2) *flat erosion:*

$$\begin{aligned}\mathrm{FE}(\mathbf{x}, N) &= \mathbf{x} \ominus \{0, n = -N, \cdots, N\} \\ &= \{\min_{n=-N,\cdots,N} (x_{i-n})\},\end{aligned}$$

which can also be interpreted as order statistical operators (the maximum filter and the minimum filter, respectively) [29].

2) Morphological Edge Operators: Morphological edge operators are written in terms of the above-defined gray scale morphological operators [20]–[23] (here we consider only versions with flat structuring element):

1) *dilation gradient:*

$$\mathrm{DG}(\mathbf{x}, N) = \mathrm{FD}(\mathbf{x}, N) - \mathbf{x};$$

2) *erosion gradient:*

$$\mathrm{EG}(\mathbf{x}, N) = \mathbf{x} - \mathrm{FE}(\mathbf{x}, N);$$

3) *Beucher's operator:*

$$\begin{aligned}\mathrm{BO}(\mathbf{x}, N) &= \mathrm{EG}(\mathbf{x}, N) + \mathrm{DG}(\mathbf{x}, N) \\ &= \mathrm{FD}(\mathbf{x}, N) - \mathrm{FE}(\mathbf{x}, N);\end{aligned}$$

4) *van Vliet's Laplacian:*

$$\begin{aligned}\mathrm{VVL}(\mathbf{x}, N) &= \mathrm{DG}(\mathbf{x}, N) - \mathrm{EG}(\mathbf{x}, N) \\ &= \mathrm{FD}(\mathbf{x}, N) + \mathrm{FE}(\mathbf{x}, N) - 2\mathbf{x};\end{aligned}$$

5) *blur and minimum operator:*

$$\mathrm{BMO}(\mathbf{x}, N) = \min\left[\mathrm{DG}(\mathbf{y}, N), \mathrm{EG}(\mathbf{y}, N)\right];$$

where $\mathbf{y}$ is a blurred version of $\mathbf{x}$ (hence, the term *blur*), obtained by some low-pass filter, and min stands for the pointwise minimum of the two involved sequences. More detailed descriptions of these morphological operators and of their characteristics can be found in [21] (DG, EG, BO, and VVL), [22] (VVL), and in [23] (DG, EG, and BMO).

3) Choice of the Most Adequate Edge Operator: All of the above-referred operators were devised to detect ideal step edges. Their performance with different types of edges has to be further studied. Accordingly, a set of increasingly difficult, i.e., increasingly realistic, tests were performed with the goal of choosing the most adequate operator among the above-considered ones.

In the first test, an ideal vessel cross-section projection is used. This would be the case of a vessel with a perfectly circular (or elliptic) cross-section, observed by a noise-free imaging system with infinite spatial resolution. The integral projection of a circle or ellipse is given by

$$p(t) = \begin{cases} \dfrac{2A}{\pi r^2}\sqrt{r^2 - (t-c)^2} & \Leftarrow |t-c| \le r \\ 0 & \Leftarrow |t-c| > r, \end{cases} \tag{3}$$

where A is its area, c the projection of its center, and r a parameter which depends on the minor and major axes (in the case of a circle, r is the radius); for details, see [12]. Such an ideal cross-section projection profile, with $c = 50$ and $r = 20$,

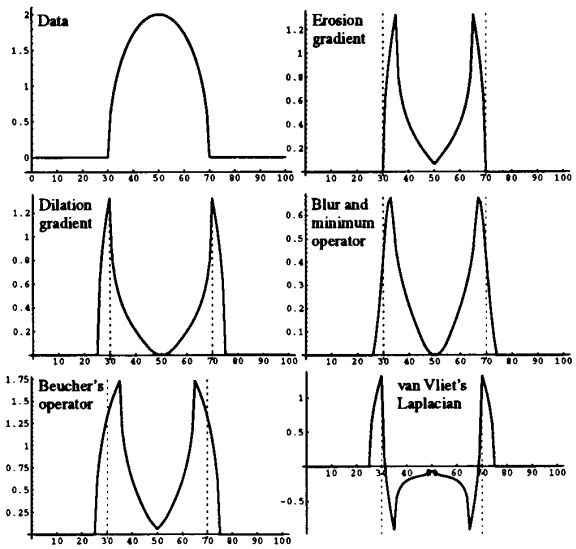

Fig. 1. Intensity profile of an ideal vessel cross-section projection and the outcomes of the five morphological edge operators considered (the vertical dashed lines signal the true location of the boundaries).

was processed with the five morphological edge operators; the results are reported in Fig. 1 (the vertical dashed lines signal the true boundary locations). In this simple setting, only two operators presented maxima at the true location of the borders: the *dilation gradient* and *van Vliet's* Laplacian.

The DG is designed to exhibit a maximum at the "*lower side*" of an ideal step edge and zero elsewhere. However, it is easy to verify that this operator is very robust against departures from ideality in the "*upper part*" of the edge, i.e., it still presents maxima on the " *lower side*" of other types of edges; this justifies the result here obtained. Moreover, the location of the maximum on the "*lower side*" of the edge makes the DG adequate to vessel border detection. The VVL, being a Laplacian, is supposed to present a zero-crossing at the location of an ideal step edge [22]; since this test considers another shape, the zero-crossing of the VVL's output is shifted towards the "*upper side*" of the edge. In any case, the VVL presents a maximum at the desired location, which is clearly due to the DG which is part of its definition (see above). Following this considerations, it is pointless to consider these two operators as competing candidates; *dilation gradient* is the most adequate operator for our purpose. To confirm this choice further tests were, however, performed.

A more realistic situation was used for the second test which is exemplified in Fig. 2. The ideal cross-section was superimposed on a ramp to simulate a nonflat background; the result was then contaminated by additive white Gaussian noise and low-pass filtered to model a true imaging system (nonzero noise and finite spatial resolution). With this data the *dilation gradient* presented maxima at the true border locations; this was consistently observed for various noise powers and (low-pass filter) bandwidths.

Tests with real cross-section profiles were also performed. In this case, one can not be sure about the true location of the

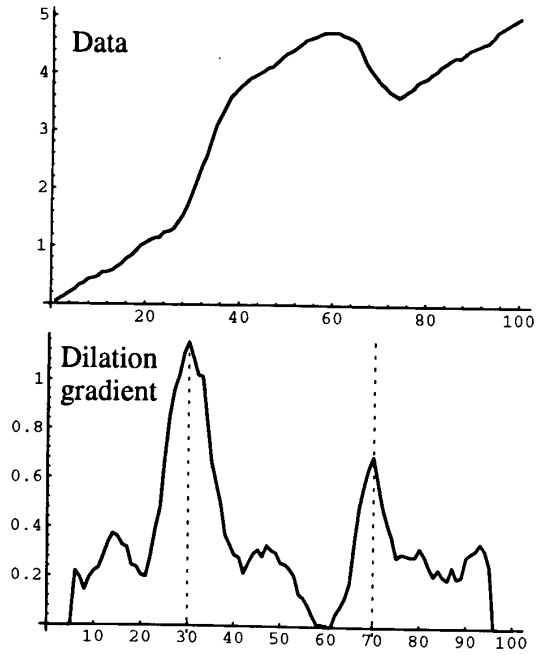

Fig. 2. Simulation of a more realistic situation: the ideal profile of Fig.1 is contaminated by additive noise, superimposed on a ramp, and finally blurred. The output produced by the *dilation gradient* morphological operator is shown (the vertical dashed lines signal the true location of the boundaries).

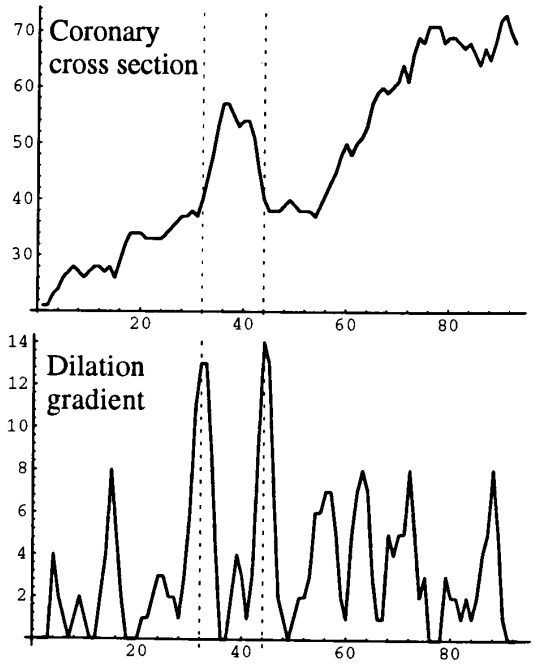

Fig. 3. True profile obtained from a coronary angiogram and, again, the output produced by the *dilation gradient* morphological operator (the vertical dashed lines signal the location of the boundaries estimated by a human observer).

vessel borders; however, the DG always produced maxima at, or very near, the locations that human observers point as being the vessel borders. One example is presented in Fig. 3, where the vertical dashed lines signal the location of the boundaries estimated by a human observer.

As a final comment, it should be said that the adopted operator is the most adequate only among the considered ones; it is, of course, not ideal and it is possible, in principle, to devise other more special-purpose detectors. Considering the ideal profile (3), a matched detector could be derived; however, since true vessel profiles exhibit a great variety of different shapes, we chose to use a simple edge detector (the *dilation gradient*) with a small structuring element ($N = 5$) which is robust against variations in the exact shape of the edge.

4) The Top-Hat Operator: Another morphological filter herein used is Meyer's *top-hat operator* (THO) [20], [21]. Since it is able to detect local elevations on arbitrary background, we employ it to detect the vessel location. The 1-D version of the THO (with flat structuring element) is defined as

$$\mathrm{THO}(\mathbf{x}, N) = \mathbf{x} - \mathrm{FD}(\mathrm{FE}(\mathbf{x}, N), N) \tag{4}$$

$$= \mathbf{x} - \{\max_{n=-N,\cdots,N} \{\min_{k=-N,\cdots,N} (x_{i-n+k})\}\}. \tag{5}$$

In Fig. 4, we present an example of what is obtained by applying this operator to a vessel cross-section intensity profile.

More sophisticated versions of the *top-hat* operator, aiming at vessel enhancement in 3-D visualization of MRA, were proposed by Vandermeulen *et al.* [19]. In that work, special

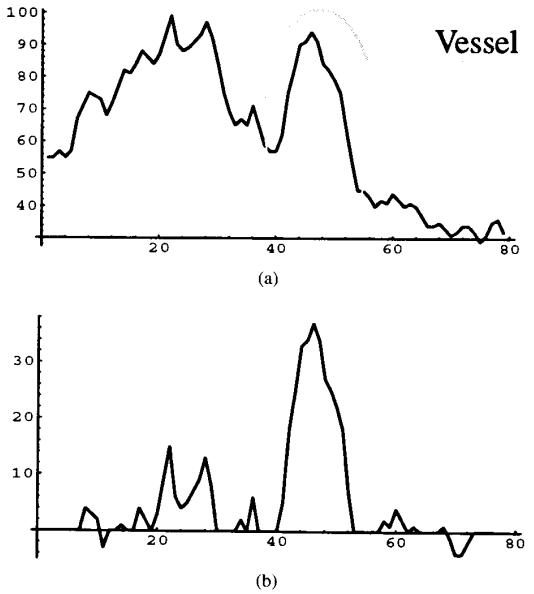

Fig. 4. (a) Intensity profile of a true coronary cross-section. (b) Outcome of the *top-hat* morphological operator (THO).

care is put on the design of a *top-hat-like* filter *matched* to vessel enhancement. Here, since the output of the *top-hat* operator is just the input of a global optimization procedure, and since we are dealing with separate (1-D) cross-sections, we settle for the original version.

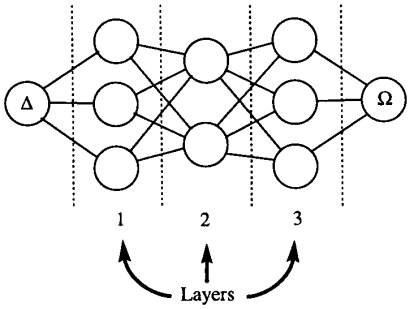

Fig. 5. Graph with a layered structure.

B. Dynamic Programming and the Shortest Path Algorithm

The *shortest path* problem is classic in combinatorial optimization; given a graph, i.e., a set of nodes linked by arcs, each with a certain *cost* or *length*, the problem consists in finding the least cost path (or *shortest path*) between each pair of nodes [24], [30].

1) Undirected Graphs: An undirected graph $\mathcal{G} = (N, A)$ is formed by a finite and nonempty set N of nodes and a collection A of distinct node pairs from N. Each element of A, i.e., each node pair, is called an arc. An arc involving nodes i and j is denoted by (i, j) and, in the case of undirected graphs, is viewed as an unordered pair. If $(m, n) \in A$, it is said that nodes m and n are adjacent. The set of all nodes adjacent to a given node i is denoted by $A(i)$. The number of nodes and arcs in a graph are denoted by $|N|$ and $|A|$, respectively [30]. Each arc (i, j) has an associated cost, or *length*, denoted by A_{ij}. If the graph is undirected $A_{ij} = A_{ji}$. A *path* from node i to node j is a sequence of adjacent nodes which starts at node i and ends at node j: $(i, n_1, n_2, \cdots, n_k, j)$ with $k \geq 0$ (if $k = 0$, the path coincides with arc (i, j)). Clearly, a path $(i, n_1, n_2, \cdots, n_k, j)$ from i to j is also a sequence of arcs $[(i, n_1), (n_1, n_2), \cdots, (n_k, j)]$. The cost of a given path is defined as the sum of the costs of all the traversed arcs.

2) The Bellman-Ford Algorithm: Assume only connected graphs, i.e., those with paths between any two nodes, and consider the problem of finding the minimum cost (or *shortest*) path between given node pairs. It is easy to prove that if all arcs have positive costs, no shortest path between any two nodes can contain the same node twice [30]. The shortest path problem is a particular instance of the more general problem of sequential decision making, or dynamic programming, for which the Bellman-Ford algorithm provides an iterative solution [24], [30].

Consider the problem of finding the shortest path from all nodes of a graph to a special one called *destination node*, e.g., take it as node 1. Denote by $x_i^\star$ the shortest path between node i and the destination node. Let x_i^k be the estimate of $x_i^\star$ at iteration k of the algorithm. The kth iteration of the Bellman-Ford algorithm is

$$x_1^k = 0 \tag{6}$$

$$x_i^k = \min_{j \in A(i)} (A_{ij} + x_j^{k-1}), \quad i = 2, 3, \cdots, |N|. \tag{7}$$

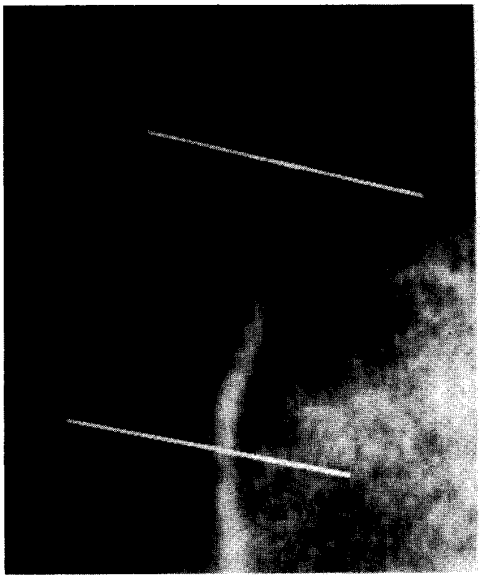

Fig. 6. Angiographic image of a portion of the coronary tree of which the section selected for analysis is delimited by two straight lines.

The initial conditions are $x_1^0 = 0$ and $x_i^k = +\infty$, for $i = 2, 3, \cdots, |N|$. The algorithm terminates when $x_i^k = x_i^{k-1}$ for all i. The Bellman-Ford algorithm converges, after at most $|N|$ iterations, and the shortest paths are its unique fixed points [30].

3) A Simplified Version of the Bellman-Ford Algorithm: The graphs we will be dealing with in this paper have a special layered structure which is depicted in Fig. 5. There are no arcs between nodes in the same layer, the nodes of a given layer are connected to all nodes of the two adjacent layers, and the extreme layers (the first and the last) have only one node (see Fig. 5). Furthermore, we are only interested in finding the shortest path between the two extreme nodes (denoted as Δ and Ω in Fig. 5). This structure can be exploited to yield a simpler and faster scheme than the general Bellman-Ford algorithm. It is clear that it is not necessary to perform Bellman-Ford iterations with all nodes simultaneously. We can start with the nodes of layer 1, which clearly converge after the first iteration, then update the nodes of the second layer, and so proceed to the last layer, and finally to node Ω. When node Ω is reached, the shortest path from Δ to Ω is determined.

V. The Algorithm

A. Description

The proposed algorithm is based on the tools presented in the previous section. It is composed of several steps, as follows:

1) Step 1: A human operator defines two cross-sections which delimit the vessel segment to be studied. These two cross-sections, which need not be parallel, constitute the only user input provided to the algorithm. This selection, an example of which is shown in Fig. 6, has some restrictions:

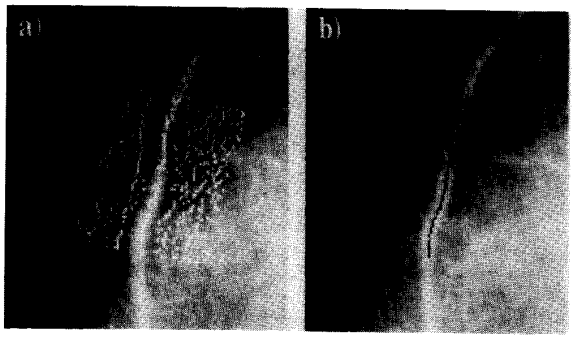

Fig. 7. (a) Vessel center candidates, i.e., maxima of the *top-hat* operator; (b) vessel skeleton, i.e., the least cost path through the candidates, obtained by the simplified Bellman-Ford algorithm described in the text.

there should be no bifurcations between the two end cross-sections; there must be only one vessel of similar intensity; and the segment should be relatively straight so that all cross-sections are approximately perpendicular to the vessel (we will refer to this issue again). All these conditions are usually met in QCA.

2) Step 2: N equispaced (in angle and distance) cross-sections of the vessel segment under study are then obtained, producing N intensity profiles $\mathbf{x}_i$, $i = 1, 2, \cdots, N$, where $\mathbf{x}_i = \{x_{ij}, j = 1, 2, \cdots, L_i\}$. These intensity profiles may contain different numbers of image samples.

3) Step 3: For each cross-section, a set of center candidates containing all the local maxima of a 1-D *top-hat* operator (THO) is determined. This set is $\mathbf{C} = \{c_{ij}, i = 1, 2, \cdots, N; j = 1, \cdots, M_i\}$ where M_i is the number of center candidates found in cross-section i. The candidates corresponding to the vessel segment of Fig. 6 are presented in Fig. 7(a). Notice that some candidates were generated by background structures (such as other vessels), while some others are caused by noise. Each center candidate is characterized by two features: $c_{ij} = (T(c_{ij}), P(c_{ij}))$, where $T(c_{ij})$ is the value of the THO at its location and $P(c_{ij})$ is the candidates position along the corresponding scan line.

4) Step 4: With the center candidates, a layered graph of the type described in Section IV-B (see Fig. 5) is built as follows: each candidate corresponds to a node; each node of a given layer (cross-section) is connected to all nodes of the two adjacent layers; and there are no arcs between nodes in the same layer. The arcs connecting two nodes (say, candidates j and k in consecutive cross-sections i and $i+1$) have a cost function which is defined as

$$A_{(ij),(i+1k)} = \alpha|P(c_{ij}) - P(c_{i+1k})| - \tfrac{1}{2}(T(c_{ij}) + T(c_{i+1k})). \quad (8)$$

This cost is tailored to increase with the distances between the candidates and decrease with the candidates THO response intensities. Two virtual nodes are created, one before the first cross-section (connected via zero-weight arcs to all nodes of the first cross-section) and the other after the last one (connected via zero-weight arcs to all nodes of the last cross-section); these nodes are termed Δ and Ω and will serve as origin and destination of the path to be found through the graph. The graph's structure is depicted in Fig. 8.

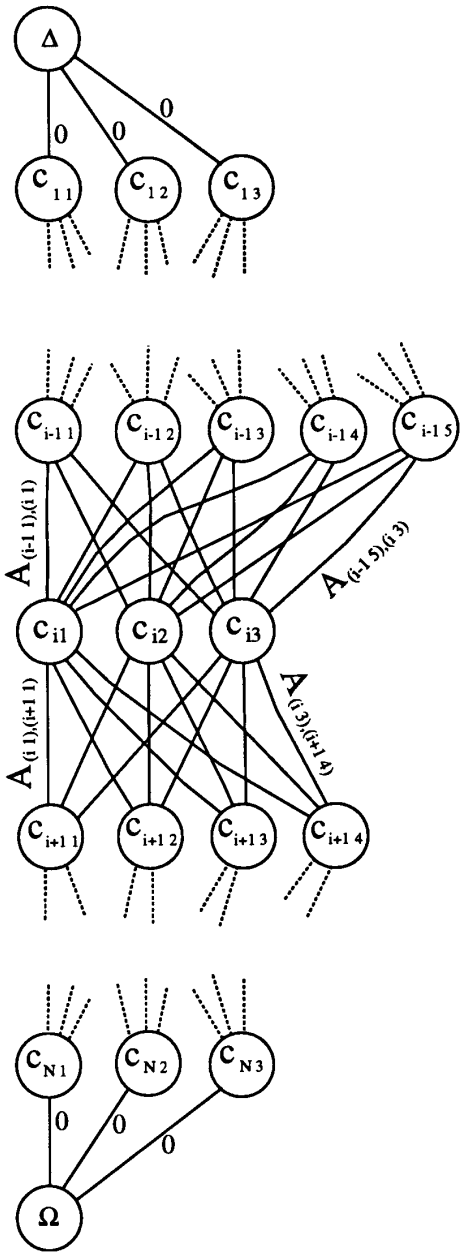

Fig. 8. Structure of the layered graphs built with the candidates.

5) Step 5: The minimum cost path along the graph, i.e., along the vessel, from Δ to Ω, is obtained by using the simpler version of the Bellman-Ford algorithm presented in the previous section. The graph's structure ensures that only one candidate is chosen from each cross-section yielding the so-called vessel *skeleton*. In Fig. 7(b), the result obtained from the candidates of Fig. 7(a) is presented. Although some candidates outside the vessel had high THO response, contextual information allowed the correct ones to be elected.

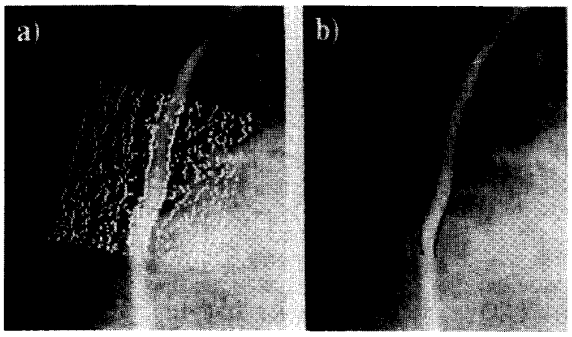

Fig. 9. (a) Vessel border candidates which are the maxima of the *dilation gradient* morphological operator; (b) vessel borders obtained from the candidates as the least cost paths (found by the simplified Bellman-Ford algorithm described in the text) through the candidates on each side of the skeleton.

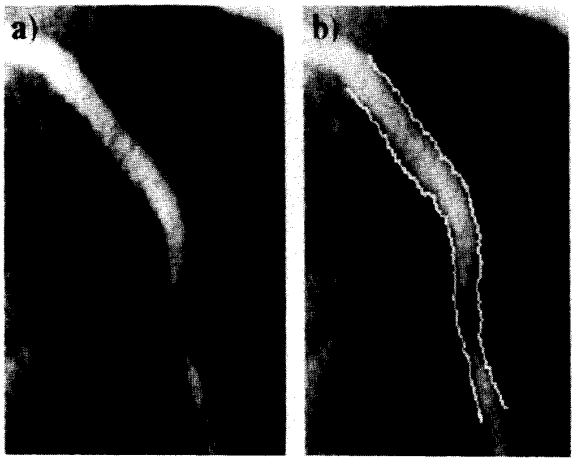

Fig. 10. (a) Original image. (b) Vessel contours obtained by the proposed algorithm.

6) Step 6: For each cross-section, two sets of border candidates are created, each containing all the maxima of a *dilation gradient* (DG) applied to each side of the vessel skeleton (see Fig. 9(a)). These sets are $\mathbf{D} = \{d_{ij},\ i = 1, 2, \cdots, N;\ j = 1, \cdots, L_i\}$ and $\mathbf{E} = \{e_{ij},\ i = 1, 2, \cdots, N;\ j = 1, \cdots, J_i\}$, where L_i and J_i are the number of border candidates found in cross-section i, to each side of the skeleton. Notice that there are more border candidates than there were center candidates; this is due to the fact that the DG, being an edge operator, has a differentiating nature thus being more sensitive to noise than the top-hat operator. Each border candidate is characterized by two features: $d_{ij} = (B(d_{ij}), P(d_{ij}))$, and $e_{ij} = (B(e_{ij}), P(e_{ij}))$, where $B(d_{ij})$ is the value of the DG at its location and $P(d_{ij})$ is the candidate's position along the corresponding scan line.

7) Step 7: These two sets of candidates are used to build two graphs similar to the one above. The arcs connecting two nodes (say, candidates j and k in consecutive cross-sections i and $i+1$) have a cost defined by

$$A_{(ij),(i+1k)} = \beta|P(d_{ij}) - P(d_{i+1k})| - \tfrac{1}{2}(B(d_{ij}) + B(d_{i+1k})). \quad (9)$$

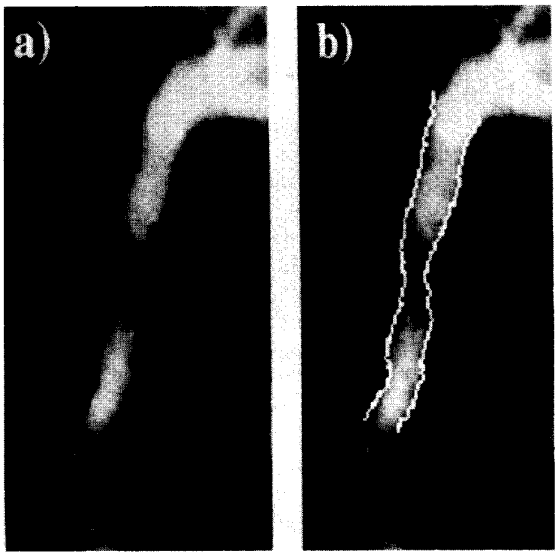

Fig. 11. (a) Original image. (b) Vessel contours obtained by the proposed algorithm.

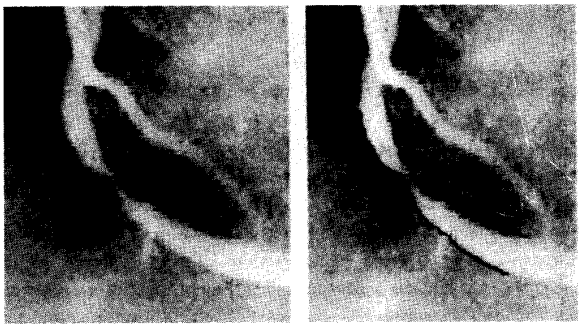

Fig. 12. (a) Original image. (b) Vessel contours obtained by the proposed algorithm.

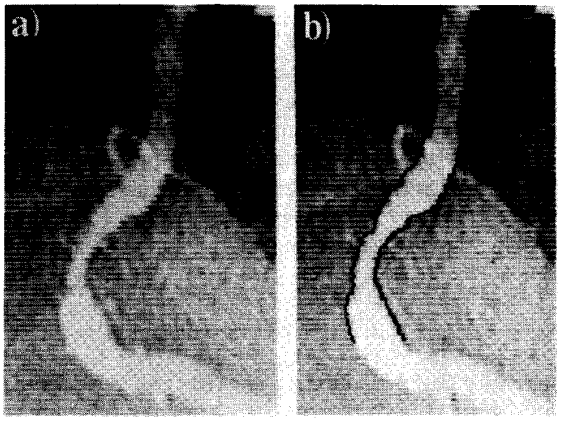

Fig. 13. (a) Original image. (b) Vessel contours obtained by the proposed algorithm.

This cost increases with the distances between the candidates and decreases with the candidate's DG strengths. As above,

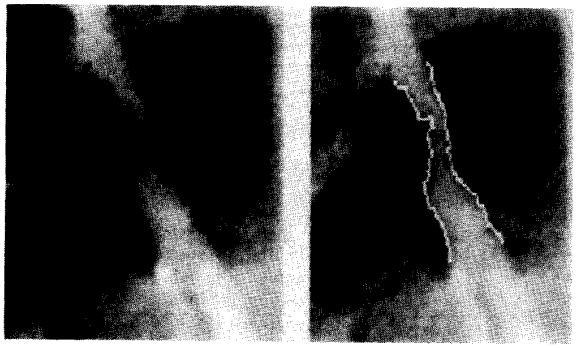

Fig. 14. (a) Original image. (b) Vessel contours obtained by the proposed algorithm.

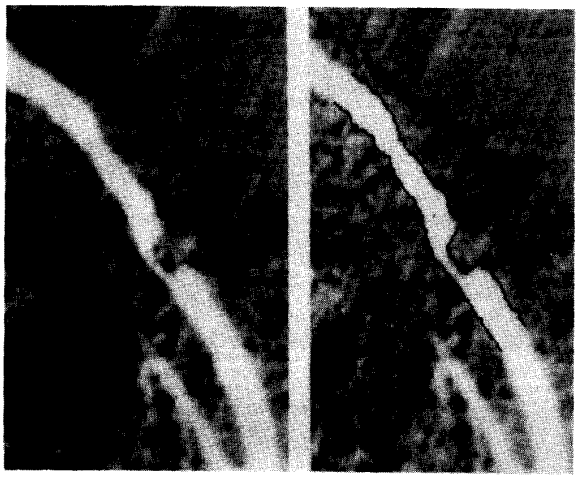

Fig. 15. (a) Original DSA image. (b) Vessel contours obtained by the proposed algorithm.

virtual nodes are created to serve as origin and destination of the paths to be found through the graphs. The structure of the obtained graphs are again similar to the one depicted in Fig. 8.

8) Step 8: Using again the simple version of the Bellman-Ford algorithm, two minimum cost paths are obtained which are the final vessel borders estimates; these are shown in Fig. 9(b).

B. Some Remarks

A few remarks concerning the proposed scheme should be made:

- Notice that the continuity terms of the cost functions (8) and (9) use L_1 norms (absolute value of the difference) which contribute to the nonsmoothing nature of the proposed estimator. This is due to the intimate relation between L_1 (robust) estimation and (step preserving) median filtering (see, e.g., [29]).
- The THO basically detects elevations smaller than its structuring element; therefore, care has to be put on the choice of its dimension N. This is especially important in areas where the cross-sections are not perpendicular to the vessel, since there it appears wider than it really is. The simplest solution is to use a large value for N; the only drawback is that the larger the THO structuring element

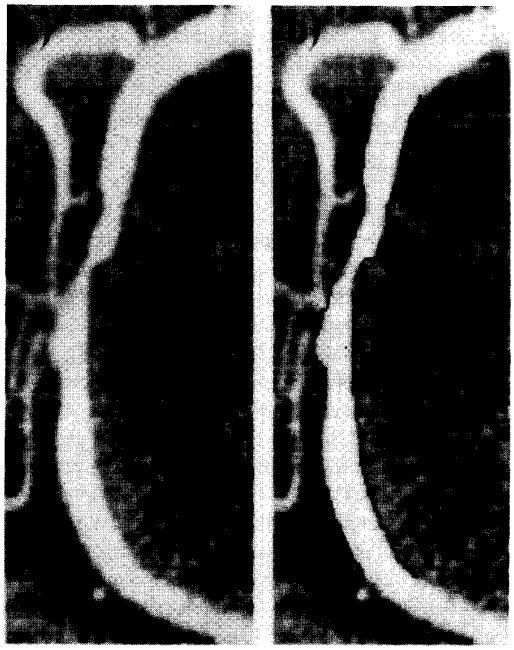

Fig. 16. (a) Original DSA image. (b) Vessel contours obtained by the proposed algorithm.

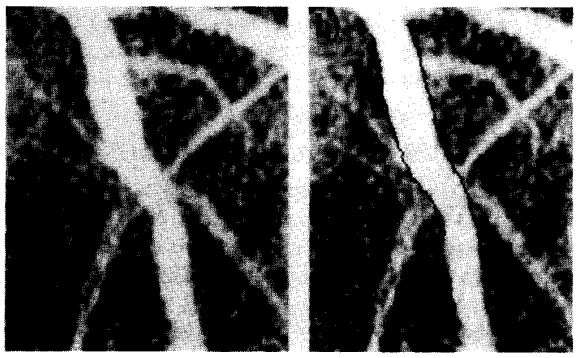

Fig. 17. (a) Original DSA image. (b) Vessel contours obtained by the proposed algorithm.

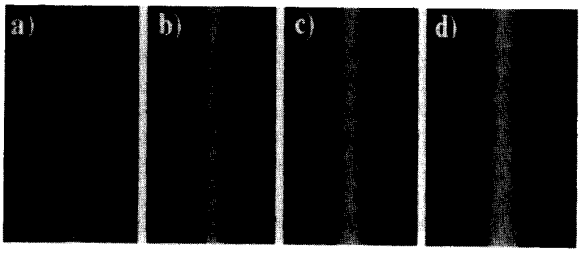

Fig. 18. Edges estimated on simulated phantoms with constant diameters of 14, 18, 22, and 30 pixels, respectively.

TABLE I
RESULTS OF THE SIMULATED PHANTOM TESTS OF FIG. 18

true diameter	14	18	22	30
mean estimated diameter	14.2	18.1	22.2	29.9
standard deviation	0.41	0.44	0.40	0.41

is, the more center candidates will obviously be generated. However, the sole consequence will be a higher burden on the (modified) Bellman-Ford algorithm since it will be dealing with a larger graph. Another option would be to use a more specialized 2-D THO (as in [19]) which, at the cost of a higher complexity, would generate a much better candidate set. There is clearly a trade-off between the performance of the operator used to generate the candidates and the load put upon the global optimization step; we chose to keep the first step as simple as possible.

- Concerning border detection, the issue of nonperpendicularity of the cross-sections is not as important; in fact, whichever the orientation of the vessel relatively to the 1-D *dilation gradient* is, its intensity profile will always present the same type of shape (only its width will vary). The DG, being a differential type local operator, will generate border candidates at the true border locations independently of its orientation (of course, within reasonable limits). Once the vessel borders are estimated, perpendicular cross-sections must be obtained for measuring purposes (geometric width and video-densitometric cross-section area).

VI. IMPLEMENTATION AND EXAMPLES

The method was implemented and tested on a common workstation where it typically takes from 2 to 10 s, thus being perfectly compatible with routine use. The computation time strongly depends on the total number of candidates produced by the morphological operators. Typically, we have 50 to 150 cross-sections, 5 to 50 center candidates and border candidates (at each side) per cross-section. This leads to graphs with 250 to 7500 nodes and the fast computation times achieved are due to the simpler version of the Bellman-Ford algorithm used.

In all the examples next presented, the parameters α in (8) and β in (9) were kept constant and both equal to 2.0. We found that, for a very wide range of situations, these values lead to good results; moreover, the obtained borders do not depend strongly on these parameters and values between 1.0 and 5.0 lead (almost always) to similar results. The widths of the *dilation gradient* and *top-hat* operators were also kept constant at $N = 5$ and $N = 23$, respectively. Figs. 10–17 present eight examples illustrating the proposed technique in several types of situations, using real angiographic images:

- Nonsubtracted angiograms, acquired from cine-film, are presented in Figs. 10–14. Images from *digital subtraction angiography* (DSA) are used in the examples of Figs. 15–17. Notice that DSA images, due to the background subtraction operation, present higher contrast, but also stronger noise.

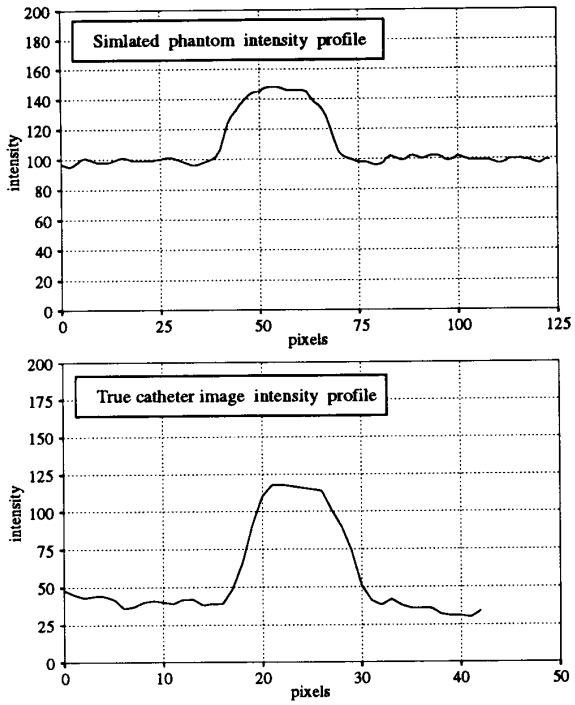

Fig. 19. Cross-sectional intensity profiles of one of the simulated phantoms of Fig. 18 and of a true catheter image.

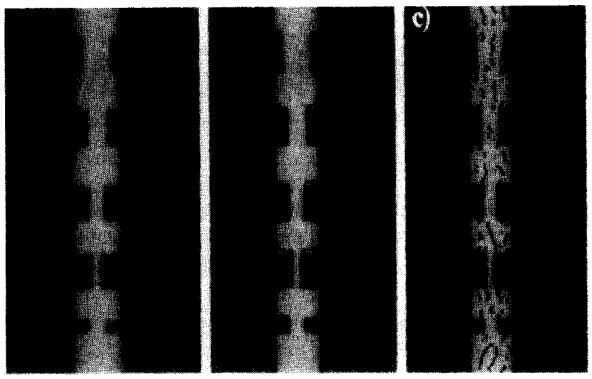

Fig. 20. (a) Simulated phantom with several abrupt stenoses; (b) estimated contours; and (c) candidates from which the contours were obtained.

- In Figs. 10–12, three rather conventional situations are presented showing smooth stenoses which were easily detected by the algorithm.
- The examples of Figs. 14 and 15 show abrupt stenoses, i.e., the vessel border exhibits sharp steps. This type of stenoses could never be correctly determined by any smoothing approach.
- The ability of the proposed technique to ignore weaker/smaller vessels is evidenced in the examples of Figs. 13, 16, and 17. These smaller vessels can even cross the main vessel, as is the case in Figs. 13 and 17.

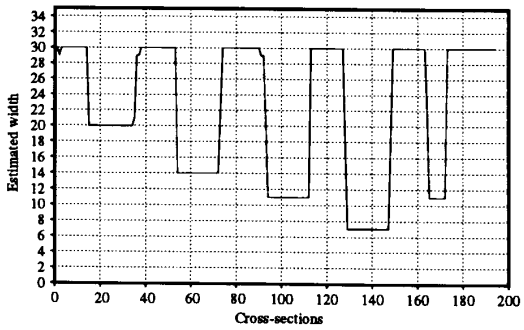

Fig. 21. Width estimated along the simulated phantom of Fig. 20.

All the contour estimates presented were considered, by expert cardiologists, as correctly obtained.

In the last two examples, we use simulated phantoms (synthetic images) aiming at providing quantitative results. Fig. 18 shows four ideal straight "*vessels*" (with diameters 14, 18, 22, and 30 pixels) and the corresponding detected borders; quantitative results (in terms of mean estimated width and standard deviation) are presented in Table I. The images were contaminated by additive noise (standard deviation equal to 10 gray levels) and blurred by a 9 × 9 Gaussian-shaped low-passed filter. These conditions were adjusted to obtain cross-section intensity profiles similar to those exhibited by true catheters in real images. For comparison purposes, Fig. 19 presents cross-sectional intensity profiles of one of the simulated phantoms and of a true catheter.

The last example includes simulated "*stenoses*" of several widths (20, 14, 11, 7, and 11, respectively, from top to bottom); the image was degraded in the same way as the images of Fig. 18. In Fig. 20(a), the original image is presented; Fig. 20(b) displays the final estimated edges obtained from the border candidates of Fig. 20(c). The estimated widths along the simulated phantom are plotted in Fig. 21. This example aims at putting in evidence the ability of the proposed technique to follow abrupt changes (which could not be achieved by any smoothing approach), and to precisely measure stenoses widths.

We point out that the examples and results presented in this section are not a full validation study; the purpose was only to illustrate the behavior of the algorithm (both qualitatively and quantitatively) in several situations.

VII. Concluding Remarks

Any vessel border estimation technique aiming at being used for QCA must undergo careful validation. Of particular importance is the study of the sensitivity of the method to image characteristics, since the quality of angiographic images spans a very wide range of levels [5]. The scope of this paper does not include such a validation, which is under way by using both phantoms and *in vivo* studies; our aim is rather to describe the concepts and tools that make up the proposed method. Of special interest, from our point of view, is the demonstration of how a dynamic programming type strategy can be used to obtain robust, albeit nondistorted, estimates. The particular edge operator adopted does not affect this aspect of the approach; other choices can easily be adopted to replace the dilation gradient. Nevertheless, we have shown that this morphological operator performs well and is adequate to the problem's specific characteristics.

Acknowledgment

The work here reported was developed in cooperation with Drs. R. Seabra-Gomes, T. Real, and J. Baptista from Hospital de Santa Cruz and Instituto do Coração. The authors acknowledge their fruitful and insightful help.

References

[1] M. Figueiredo and J. Leitão, "An unbiased technique for automatic estimation of vessel contours in angiograms," in *Proc. IEEE Nucl. Sci. Sympos. Med. Imag. Conf.*, San Francisco, CA, pp. 1251–1254, 1993.

[2] J. Reiber, C. Kooijman, C. Slager, J. Gerbrands, J. Schuurbiers, A. Boer, W. Wijns, P. Serruys, and P. Hugennholtz, "Coronary artery dimensions from cineangiograms—Methodology and validation of a computer assisted analysis procedure," *IEEE Trans. Med. Imag.*, vol. MI-3, pp. 131–141, 1984.

[3] J. Reiber and P. Serruys, *Advances in Quantitative Coronary Arteriography*. Dordrecht, The Netherlands: Kluwer Academic Publ., 1993.

[4] ——, "Quantitative coronary arteriography," in *Cardiac Imaging*, M. Marcus, D. Skorton, H. Schelbert, G. Wolf, and E. Braunwald, Eds. Philadelphia, PA: W. B. Saunders Co., 1991, pp. 211–280.

[5] S. Fleagle, M. Johnson, C. Wilbricht, D. Skorton, R. Wilson, C. White, M. Marcus, and S. Collins, "Automated analysis of coronary arterial morphology in cineangiograms: Geometric and physiologic validation in humans," *IEEE Trans. Med. Imag.*, vol. 8, pp. 387–400, 1989.

[6] D. Pope, D. Parker, D. Gustafson, and P. Clayton, "Dynamic search algorithms in left ventricular border recognition and analysis of coronary arteries," in *Proc. Comput. in Cardiol.*, pp. 71–75, 1984.

[7] P. Eichel, E. Delp, K. Koral, and A. Buda, "A method for a fully automatic definition of coronary arterial edges from cineangiograms," *IEEE Trans. Med. Imag.*, vol. 7, pp. 313–320, 1988.

[8] Y. Sun, "Automated identification of vessel contours in coronary arteriograms by an adaptive tracking algorithm," *IEEE Trans. Med. Imag.*, vol. 8, pp. 78–88, 1989.

[9] M. Figueiredo and J. Leitão, "Bayesian estimation of ventricular contours in angiographic images," *IEEE Trans. Med. Imag.*, vol. 11, pp. 416–429, 1992.

[10] Y. Bresler and A. Macowski, "Three-dimensional reconstruction from projections with incomplete and noisy data by object estimation," *IEEE Trans. Acoust., Speech, Signal Process.*, vol. ASSP-35, pp. 1139–1152, 1987.

[11] D. Rossi and A. Willsky, "Reconstruction from projections based on detection and estimation of objects," *IEEE Trans. Acoust., Speech, Signal Process.*, vol. ASSP-32, pp. 886–906, 1984.

[12] T. Pappas and J. Lim, "A new method for estimation of coronary artery dimensions in angiograms," *IEEE Trans. Acoust., Speech, Signal Process.*, vol. 36, pp. 1501–1513, 1988.

[13] A. Nichols, C. Gabrieli, J. Fenoglio, and P. Esser, "Quantification of relative coronary artery stenosis by cinevideodensitometric analysis of coronary arteriograms," *Circ.*, vol. 69, pp. 512–522, 1984.

[14] D. Parker, D. Pope, J. Petersen, P. Clayton, and D. Gustafson, "Quantitation in cardiac videodensitometry," in *Proc. Comput. in Cardiol.*, pp. 119–122, 1984.

[15] ——, "Automated evaluation of vessel diameters from arteriograms," in *Proc. Comput. in Cardiol.*, pp. 215–218, 1982.

[16] E. Alderman, L. Berte, D. Harrison, and W. Sanders, "Quantitation of coronary artery dimensions using digital image processing," in *Digital Radiography*, W. Brody, Ed. New York: SPIE, 1982.

[17] P. Doriot, Y. Pochon, and L. Rasoamanambelo, "Densitometry of coronary arteries—An improved physical model," in *Proc. Comput. in Cardiol.*, pp. 145–148, 1985.

[18] M. LeFree, M. Simon, G. Mancini, and R. Vogel, "Digital radiographic assessment of coronary arterial geometric diameter and videodensitometric cross-sectional area," in *Proc. SPIE 626*, pp. 334–341, 1986.

[19] D. Vandermeulen, D. Delaere, P. Suetens, H. Bosmans, and G. Marchal, "Local filtering and global optimization methods for 3-D magnetic resonance angiography (MRA) image enhancement," in *Visualization in Biomedical Computing*, R. Robb, Ed. Chapel Hill, NC: SPIE, 1992, pp. 274–288.

[20] J. Serra, *Image Analysis and Mathematical Morphology*. New York: Academic Press, 1988.
[21] P. Maragos and R. Schafer, "Morphological systems for multidimensional signal processing," *Proc. IEEE*, vol. 78, pp. 690–710, 1990.
[22] L. van Vliet, I. Young, and G. Beckers, "A nonlinear Laplace operator as edge detector in noisy images," *Comput. Vision, Graphics, and Image Process.*, vol. 45, pp. 167–195, 1989.
[23] J. Lee, R. Haralick, and L. Shapiro, "Morphologic edge detection," *IEEE J. Robotics Automat.*, vol. RA-3, pp. 142–156, 1987.
[24] R. Bellman, *Dynamic Programming*. Princeton: Princeton University Press, 1957.
[25] A. Amini, T. Weymouth, and R. Jain, "Using dynamic programming for solving variational problems in vision," *IEEE Trans. Pattern Anal. Mach. Intell.*, vol. 12, pp. 855–867, 1990.
[26] J. Dias and J. Leitão, "Wall position and thickness estimation from two-dimensional echocardiograms," in *Proc. IEEE Nucl. Sci. Sympos. Med. Imag. Conf.*, San Francisco, pp. 1246–1249, 1993.
[27] D. Geiger and J. Vlontsos, "Matching elastic contours," in *Proc. IEEE Comput. Soc. Conf. Comput. Vision and Pattern Recog.*, New York, pp. 602–604, 1993.
[28] D. Geiger and A. Gupta, "Detecting and tracking the left and right heart ventricles via dynamic programming," in *Medical Imaging 1994: Image Processing*, M. Loew, Ed. Newport Beach, CA: SPIE, 1994, pp. 391–402.
[29] I. Pitas and A. Venetsanopoulos, "Order statistics in digital image processing," *Proc. IEEE*, vol. 80, pp. 1893–1921, 1992.
[30] D. Bertsekas and J. Tsitsiklis, *Parallel and Distributed Computation. Numerical Methods*. Englewood Cliffs, NJ: Prentice-Hall, 1989.